small
NANO MICRO

3D Carbon/Cobalt-Nickel Mixed-Oxide Hybrid Nanostructured Arrays for Asymmetric Supercapacitors

*Jianhui Zhu, Jian Jiang, Zhipeng Sun, Jingshan Luo, Zhanxi Fan, Xintang Huang, Hua Zhang, and Ting Yu**

***T**he electrochemical performance of supercapacitors relies not only on the exploitation of high-capacity active materials, but also on the rational design of superior electrode architectures. Herein, a novel supercapacitor electrode comprising 3D hierarchical mixed-oxide nanostructured arrays (NAs) of C/$CoNi_3O_4$ is reported. The network-like C/$CoNi_3O_4$ NAs exhibit a relatively high specific surface area; it is fabricated from ultra-robust Co-Ni hydroxide carbonate precursors through glucose-coating and calcination processes. Thanks to their interconnected three-dimensionally arrayed architecture and mesoporous nature, the C/$CoNi_3O_4$ NA electrode exhibits a large specific capacitance of 1299 F/g and a superior rate performance, demonstrating 78% capacity retention even when the discharge current jumps by 100 times. An optimized asymmetric supercapacitor with the C/$CoNi_3O_4$ NAs as the positive electrode is fabricated. This asymmetric supercapacitor can reversibly cycle at a high potential of 1.8 V, showing excellent cycling durability and also enabling a remarkable power density of ~13 kW/kg with a high energy density of ~19.2 W·h/kg. Two such supercapacitors linked in series can simultaneously power four distinct light-emitting diode indicators; they can also drive the motor of remote-controlled model planes. This work not only presents the potential of C/$CoNi_3O_4$ NAs in thin-film supercapacitor applications, but it also demonstrates the superiority of electrodes with such a 3D hierarchical architecture.*

J. H. Zhu, J. Jiang, Dr. Z. P. Sun, J. S. Luo, Prof. T. Yu
Division of Physics and Applied Physics
School of Physical and Mathematical Sciences
Nanyang Technological University
637371, Singapore
E-mail: yuting@ntu.edu.sg

J. H. Zhu, J. Jiang, Prof. X. T. Huang
Institute of Nanoscience and Nanotechnology
Department of Physics
Central China Normal University
Wuhan, Hubei 430079, China

Z. X. Fan, Prof. H. Zhang
School of Materials Science and Engineering
Nanyang Technological University
639798, Singapore

Prof. T. Yu
Department of Physics
Faculty of Science
National University of Singapore
117542 Singapore Graphene Research Centre
National University of Singapore
117546, Singapore

DOI: 10.1002/smll.201302937

1. Introduction

Supercapacitors have attracted considerable attention because they can store more electric energy than conventional dielectric capacitors and because they enable superior power delivery to batteries; as a result, they have potential in a broad spectrum of applications, such as in portable electronics, power back-ups, and electrical vehicles (EVs).[1] Unfortunately, the energy density of commercially available supercapacitors is quite low (normally less than 10 W·h/kg), which is significantly far from fulfilling the ever-growing energy demands, especially for modern/next-generation portable devices and EVs.[2,3] Therefore, advanced supercapacitors that possess both a large operating voltage and superior energy density without having to sacrifice their cyclic life and power delivery need to be developed, but to date, their development remains a challenge.[4]

To best increase the energy density, several smart strategies have been tried. One strategy involves the development of advanced asymmetric supercapacitors (ASCs) with a battery-type Faradic electrode as an energy source and a

© 2014 Wiley-VCH Verlag GmbH & Co. KGaA, Weinheim

non-Faradic capacitive electrode as a power source.[5] This would combine the advantages of the two different electrode materials as well as achieve a high operation voltage in aqueous electrolytes (even up to 2 V).[5–7] Another effective way involves the development of high-capacity materials and the design of optimal electrode architecture, both of which can be used to improve supercapacitor performance.[8] Among electrode materials, transition-metal oxides can be described as "always welcoming" candidates because for most of them their transition-metal centers possess multiple accessible valence states, which would enable a variety of reversible redox reactions and thus generate high pseudocapacitance for supercapacitors.[9] Co- and Ni-based oxides (Co_3O_4, CoO, NiO) have long been considered as very promising electrode materials by means of their excellent pseudocapacitive properties, such as good redox activity and reversibility.[10,11] Particularly, their mixed-oxide forms exhibit far better electrochemical performance than either monometallic oxide due to the enhanced electrochemical reversibility and conductivity.[12,13] In addition to electrode materials, the design of advanced electrode architectures is also regarded as an important factor to boost the performance of supercapacitors.[14] In recent years, a great deal of progress in arrayed binder-free electrode architectures has been achieved; this progress includes various nanostructure (nanowire/nanorod/nanowall) arrays, coaxial hybrid nanostructures, and 3D hybrid networks, all of which can effectively avoid the "dead surface" that occurs in conventional slurry-derived electrodes and can enable more efficient charge/mass exchanges.[15–17] When compared with other architectures, 3D hierarchical network-like nanostructure arrays have attracted special attention due to their higher surface areas, increased number of active sites, and better permeability for energy-storage applications.[17,18]

Herein, we design a novel electrode comprising 3D network-like hybrid nanostructured arrays (NAs) of C/$CoNi_3O_4$ that are built directly on current collectors; the electrode exhibits good mechanical adhesion to the substrate and relatively high specific surface areas. The 3D C/$CoNi_3O_4$ NAs are prepared via a facile hydrothermal approach, followed by glucose-coating and calcination treatments. They are then applied directly as electrodes for supercapacitors, avoiding typically tedious electrode preparation. The C/$CoNi_3O_4$ NA electrode is capable of delivering a high specific capacitance of 1299 F/g (~1429 mF/cm^2) at a current rate of ~0.5 mA/cm^2. In addition, this electrode shows superior rate capability; even when the discharge current increases up to 50 mA/cm^2 (100 times that of pristine 0.5 mA/cm^2), the electrode maintains a large specific capacitance of 1018.2 F/g (1120 mF/cm^2; the capacity retention is up to ~78%). An optimized asymmetric supercapacitor is assembled by adopting C/$CoNi_3O_4$ as the energy source and activated carbon (AC) as the power source. The C/$CoNi_3O_4$//AC asymmetric supercapacitor can work at a voltage as high as 1.8 V and exhibit a capacitance of 64.7 F/g under a current density of 1 mA/cm^2. When the current reaches ~100 mA/cm^2 (fully charged/discharged in few seconds), this supercapacitor enables a remarkable power density of 13.0 kW/kg while still retaining a high energy density of up to 19.2 W·h/kg. Additionally, an exceptional cycling performance was demonstrated with negligible capacity loss after 5000 cycles. With only seconds of charging, two asymmetric supercapacitors connected in series (electrode area: 4 cm^2) can simultaneously power four different types of LED indicators and can drive the motors of remote-controlled model planes (2 V, 0.56 A), confirming the potential of these supercapacitors for practical applications.

2. Results and Discussion

The synthetic strategy used to fabricate the 3D C/$CoNi_3O_4$ hybrid NAs is schematically displayed in **Figure 1**a. Two

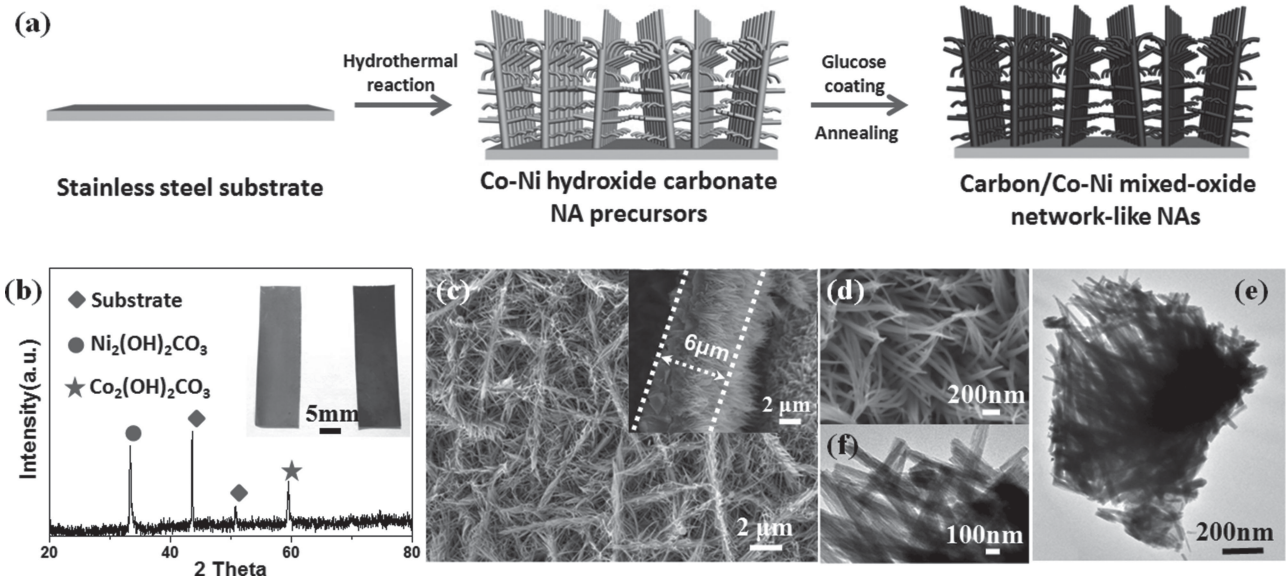

Figure 1. a) Schematic showing the preparation of the 3D C/Co-Ni mixed-oxide network-like NAs; b) XRD pattern of Co-Ni hydroxide carbonate NA precursors. Inset: optical images of the precursor (left) and final product (right); c–e) Low- and high-resolution SEM (c,d) and TEM (e,f) observations of the precursors.

© 2014 Wiley-VCH Verlag GmbH & Co. KGaA, Weinheim
small 2014,
DOI: 10.1002/smll.201302937

NANO MICRO small

main procedures are required for the entire fabrication process: i) the synthesis of 3D NAs comprising a Co-Ni mixed hydroxide carbonate on a Fe-Co-Ni substrate via a controllable one-step hydrothermal method; ii) uniform coating of the precursors with glucose molecules, followed by annealing in Ar atmosphere. The inset of Figure 1b shows the optical images of the Co-Ni hydroxide carbonate precursors and the final C/$CoNi_3O_4$ hybrid NAs, indicating that the film products can grow uniformly on the substrate at a large scale. The crystallographic structure/phase purity of the precursors was examined by powder X-ray diffraction (XRD). Aside from peaks from the metal substrate (Figure 1b), all other diffraction peaks originate from the precursors and agree well with standard XRD patterns of (Ni, $Co)_2(OH)_2CO_3$ (Joint Committee on Powder Diffraction Standards, JCPDS File: 35–0501 and 38–0547). Representative scanning electron microscopy (SEM) images (Figure 1c,d) reveal that the precursors possess an integrated 3D network-like architecture, which is constructed by interconnected nanowalls and entangled nanowires distributed on their surface. A typical cross-section SEM image (Figure 1d, inset) reveals that the thickness of the as-synthesized nanostructured film is ~6 μm on average. Transmission electron microscopy (TEM) observations (Figure 1e,f) confirm that the nanowires (diameter: ~20 nm) grow uniformly on each nanowall lamella, highly consistent with the SEM results. To ensure whether the self-standing NAs possess an effective and sustainable contact to the substrate, we conducted an ultra-sonication test (lasting 30 min) on the samples. The thin-film precursors fabricated on the alloy substrate were immersed into 80 mL of distilled water and then treated in an ultra-sonication cleaner (power: 250 W; frequency: 40 kHz).

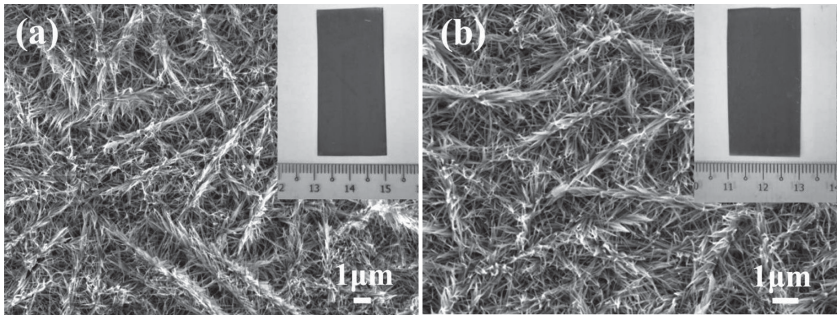

Figure 2. SEM and optical (insets) images of the Co-Ni hydroxide carbonate NA precursors a) before and b) after a 30-min ultra-sonication treatment.

Corresponding optical and SEM images are displayed in **Figure 2**. Note that after a 30-min ultra-sonication treatment, the precursor film (Figure 2b) has not peeled off of the substrate; it even retains the same network-like arrayed morphology/architecture as that of untreated samples (Figure 2a), revealing the robust mechanical adhesion between the precursor film and alloy substrate. This feature could facilitate the charge transfer process and benefit other potential electrochemical applications, such as for electrochemical sensors.

The precursors were further transformed into 3D C/$CoNi_3O_4$ hybrid NAs by means of glucose coating and then calcination. SEM images of the C/$CoNi_3O_4$ hybrid NAs (**Figure 3**a,d) illustrate that C/$CoNi_3O_4$ hybrid NAs can still maintain the geometrical morphology of the precursors without any structural exfoliation or collapse even after a high-temperature calcination treatment. It is noted that a great deal of void space is uniformly dispersed within the top-open network nanostructures, greatly facilitating ionic diffusion especially at a high charging/discharging rate. A high-resolution SEM image (Figure 3d) reveals a large quantity of pores distributed throughout the surface of the nanowires. This would mainly rely on the pyrolysis of the

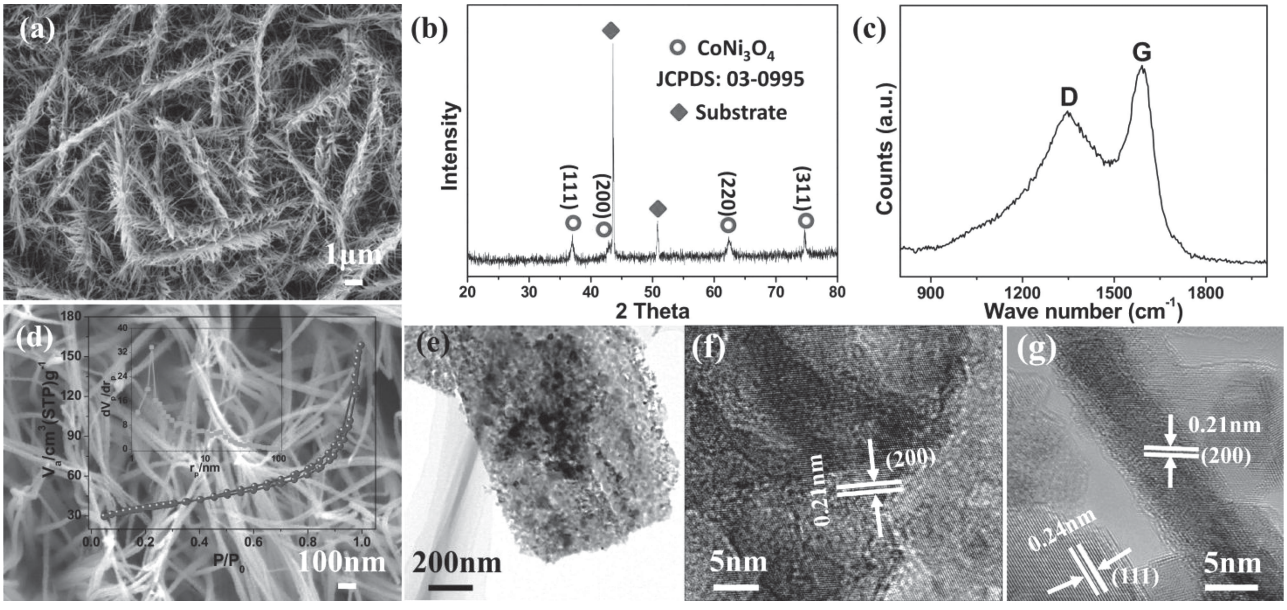

Figure 3. a) SEM image, b) XRD plot, c) Raman spectrum, d) high-resolution SEM image, and e–g) TEM and HRTEM images of the final product of C/$CoNi_3O_4$. Inset of (d) is the N_2-adsorption/desorption isotherms and pore-size distribution of C/$CoNi_3O_4$ at 77 K.

DOI: 10.1002/smll.201302937
© 2014 Wiley-VCH Verlag GmbH & Co. KGaA, Weinheim

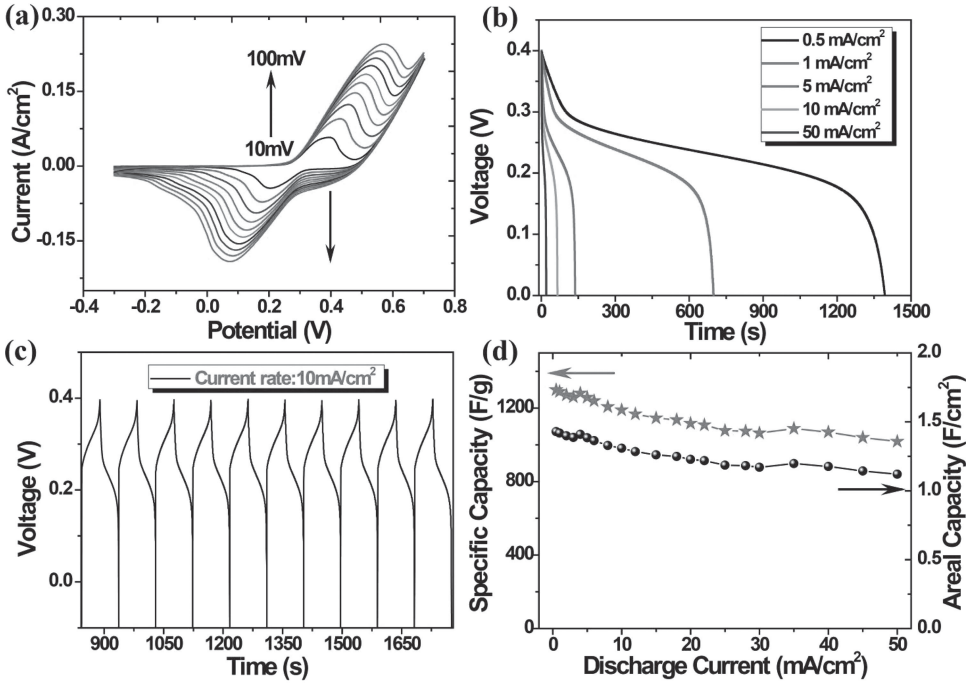

Figure 4. a) Cyclic voltammograms (where potential is versus SCE) and b) galvanostatic discharge curves of a C/$CoNi_3O_4$ NA electrode, collected at different scan/current densities in 3 m KOH. c) Galvanostatic charge/discharge plots of C/$CoNi_3O_4$ NAs measured under a current density of 10 mA/cm^2. d) Specific and areal capacitance as a function of discharge current density.

hydroxide carbonate leading to the loss of H_2O and CO_2 during the calcination process.[19] The mesoporous nature of the products was characterized using N_2-adsorption/desorption measurements. The isotherms and pore-size distribution curves (Figure 3d) reveal that our sample has type-IV N_2-adsorption/desorption isotherms with a pronounced type-H1 hysteresis loop, which typically appears in the case of mesoporous materials, with a specific surface area of 128.1 m^2 g^{-1}. This value indicates the hybrid products have a relatively high specific surface area, capable of providing sufficient electrode/electrolyte interfaces and increasing the number of reversible redox reaction sites for supercapacitors. The pore-size distribution (Figure 3d, inset) is centered at 2.1 and 16.3 nm, further confirming the mesoporous nature of the C/$CoNi_3O_4$ hybrid NAs. The total pore volume and the average pore diameter are measured to be ~29.4 cm^3 g^{-1} and 7.1 nm, respectively; such characteristics provide ions with easy access to the electrode/electrolyte interface.[20] XRD was employed to examine the final samples (Figure 3b). New diffraction peaks appearing at 2θ of 37.02°, 42.9°, 62.3°, and 74.7° are in good agreement with $CoNi_3O_4$ (JCPDS File 03–0995), corresponding the (111), (200), (220), and (311) facets, respectively. A Raman spectrum was also obtained in a wavelength range of ~800–2200 cm^{-1} (Figure 3c). Obviously, there are two broad peaks present at 1347 and 1595 cm^{-1}, which are attributed to the D and G bands of graphite, respectively; they confirm the success of the carbon coating.[21] TEM observations confirm the uniform distribution of the mesopores on each lamella (Figure 3e), and they indicate lattices of 0.21 and 0.24 nm (Figure 3f,g). These values are consistent with the (200) and (111) interplanar spacing, respectively, of $CoNi_3O_4$, and they agree with the XRD measurements.

To evaluate the electrochemical properties of C/$CoNi_3O_4$ NAs, cyclic voltammetry (CV) and chronopotentiometry (CP) measurements were conducted in a three-electrode system with a Pt plate counter-electrode and a saturated calomel reference electrode (SCE) in 3 m KOH electrolyte. **Figure 4**a shows representative CV curves of the C/$CoNi_3O_4$ NA electrode (electrode area: ~2 cm × ~0.5 cm) at various scan rates ranging from 10 to 100 mV/s. A pair of symmetric cathodic and anodic peaks are clearly observed on each CV curve within a voltage window of approximately (–0.3)–(+0.7) V. This is related to a combined effect of the reversible surface/near-surface Faradic reactions between Co^{2+}/Co^{3+} and Ni^{2+}/Ni^{3+}, suggesting the pseudocapacitive behavior of the C/$CoNi_3O_4$ NA electrode.[22] Along with the increase of scan rates, the current response/intensity is also enhanced; however, there is no significant change in the shape of cyclic voltammograms, demonstrating the good electrochemical stability of the C/$CoNi_3O_4$ hybrid NAs. To further examine the electrochemical performance, we performed constant charge/discharge measurements on the C/$CoNi_3O_4$ NA electrode at distinct current densities varying from 0.5 to 50 mA/cm^2 within a voltage window of approximately 0–(+0.4) V (Figure 4b). Unlike the case of electric double-layer capacitors (EDLCs) with linear charge/discharge characteristics, the discharge curves of the C/$CoNi_3O_4$ NA electrode show well-defined potential plateaux, illustrating a typical pseudocapacitive behavior and agreeing well with former CV results. The charge/discharge curves at a scan rate of 40 mA/cm^2 are quite symmetric (Figure 4c), which implies high Coulombic efficiency (nearly 100%) in the C/$CoNi_3O_4$ NA electrode. The specific capacitance derived from the charge/discharge plots is also calculated (Figure 4d). Under

© 2014 Wiley-VCH Verlag GmbH & Co. KGaA, Weinheim
small 2014,
DOI: 10.1002/smll.201302937

NANO MICRO small

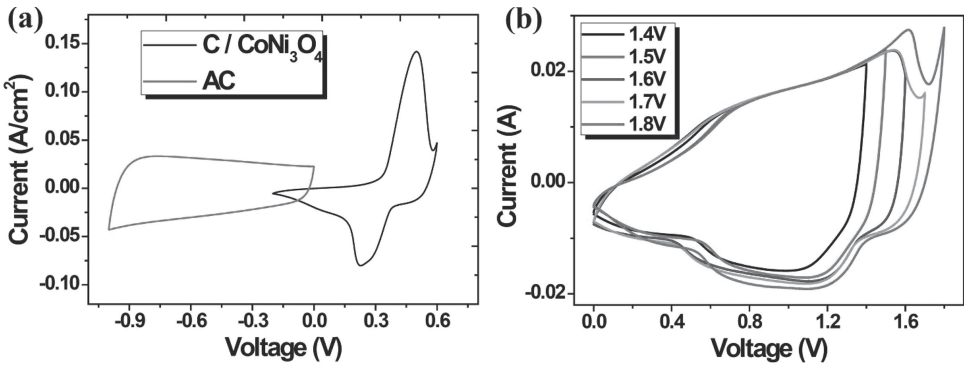

Figure 5. a) Cyclic voltammograms of the $C/CoNi_3O_4$ NA and active carbon (AC) electrodes performed in a three-electrode system in 3 M KOH solution at a scan rate of 30 mV/s. b) Cyclic voltammograms of the $C/CoNi_3O_4$//AC asymmetric supercapacitors measured with varying upper bounds to the potential window at a scan rate of 50 mV/s. Voltage is relative to SCE.

a current density of ~0.5 mA/cm^2, the measured capacitance of the $C/CoNi_3O_4$ NAs is around 1299.1 F/g (1.43F/cm^2). Even at a rate as high as ~50 mA/cm^2 (~100 times higher than the original rate of ~0.5 mA/cm^2), the hybrid electrode is still able to deliver a capacitance of 1018.2 F/g (1.12 F/cm^2); ~78.3% of the capacitance remains when current rates are sharply increased, exhibiting the excellent rate behavior of the $C/CoNi_3O_4$ NA electrode. We believe that the superior electrochemical performance is mainly attributed to the following aspects. First, the unique hierarchical 3D network-like electrode architecture provides an effective pathway for ion diffusion and electron transport because it allows for significantly shorter diffusion/migration paths for charge carriers and because it facilitates the surface-dependant Faradic processes even at a high scan/current rate.[23,24] Second, the relatively high surface area rendered by the mesoporous structures allows for an increased number of accessible reaction sites; therefore, extensive exploitation of the active materials is ensured and accordingly the specific capacitance can be largely enhanced.[23,24] Last but not least, the binder-free fabrication enables a low interfacial resistance, which is also favorable for fast electrochemical reactions.[23,24]

The capacitive behavior of the $C/CoNi_3O_4$ NA electrode in a full-cell set-up has also been investigated. A 2 cm × 0.5 cm asymmetric supercapacitor was made by using $C/CoNi_3O_4$ NAs as the cathode and AC as the anode (denoted as $C/CoNi_3O_4$//AC). Prior to testing the $C/CoNi_3O_4$//AC supercapacitor, the CV of both the cathode and anode were measured at a scan rate of 30 mV/s in a three-electrode system. The AC anode electrode was tested in a voltage window of approximately (–1.0)–(0) V (vs. SCE). As shown in **Figure 5**a, no obvious redox peaks were observed in the rectangular cyclic voltammogram, and on voltage reversal, the electrode exhibits a nearly mirror-image current response, revealing a typical characteristic of an EDLC and excellent electrochemical reversibility. The $C/CoNi_3O_4$ NA cathode was measured in a voltage window of approximately (–0.2)–(+0.6) V, wherein a couple of well-defined pseudocapacitive peaks are present. According to the above CV tests, the specific capacitance (C) of these electrodes is calculated from the equation: $C = (\int I dV/(\upsilon m V)$, where I is the response current density (A/cm^2), V is the potential (V), υ is the potential scan rate (mV/s), and m is the mass of the electroactive materials in the electrode (g).[25] The specific capacity of the $C/CoNi_3O_4$ NAs is measured to be ~855.5 F/g while that of AC is 129.8 F/g. To balance the charge storage ($Q_+ = Q_-$) between the two electrodes, the mass of the electrode materials needs to follow the equation of $\frac{m_+}{m_-} = \frac{c_- \times \Delta E_-}{c_+ \times \Delta E_+}$ (m, C, and ΔE represent the mass of the active materials, the specific capacitance, and the charge/discharge voltage of the two electrodes; and the subscripts + and – refer to the positive and negative charge carriers).[25] By referring to the specific capacitance calculated from the above CV results, ~5.8 mg of AC is required to be contained per square-centimeter of anode. Figure 5b shows the cyclic voltammogram of the $C/CoNi_3O_4$//AC asymmetric supercapacitor under different potential windows at a scan rate of 50 mV/s. It is obvious that the CV curve of the $C/CoNi_3O_4$// AC supercapacitor remains stable even when its potential window increases up to 1.8 V, and this value is nearly two times that of traditional carbon-based symmetric capacitors using aqueous electrolyte (0.8–1.0 V). Moreover, the high voltage range is favorable for improving the energy density of the supercapacitor and it enables fewer devices connected in series to reach the desired output voltage.[26] Thus, we have chosen an operation potential window of approximately 0–(+1.8) V to further study the electrochemical performance of the $C/CoNi_3O_4$//AC asymmetric supercapacitors.

Figure 6a shows cyclic voltammograms of the optimized $C/CoNi_3O_4$//AC asymmetric supercapacitor performed at various scanning rates ranging from 5 to 150 mV/s. The full-cell supercapacitor exhibits a quasi-rectangular CV geometry, indicating an EDLC-like capacitive behavior and differing from the features of the $C/CoNi_3O_4$ electrode tested in a three-electrode electrochemical system. Even when the scan rate increases to be as high as 150 mV/s, the voltammograms remain quasi-rectangular without any obvious distortions, suggesting a desirable high-rate performance for power delivery. Galvanostatic discharge curves of the $C/CoNi_3O_4$//AC supercapacitor performed at various current densities are shown in Figure 6b. Unlike the case in Figure 4b, the discharge curves of the $C/CoNi_3O_4$//AC supercapacitor exhibits nearly linear variation with the cell potential. The charge/discharge curves at a scan rate of 40 mA/cm^2 (see Figure 6c) are quite symmetric, with a linear relationship of the discharge/charge potential versus time. This demonstrates ideal capacitive characteristics and fast charge/discharge

DOI: 10.1002/smll.201302937
© 2014 Wiley-VCH Verlag GmbH & Co. KGaA, Weinheim

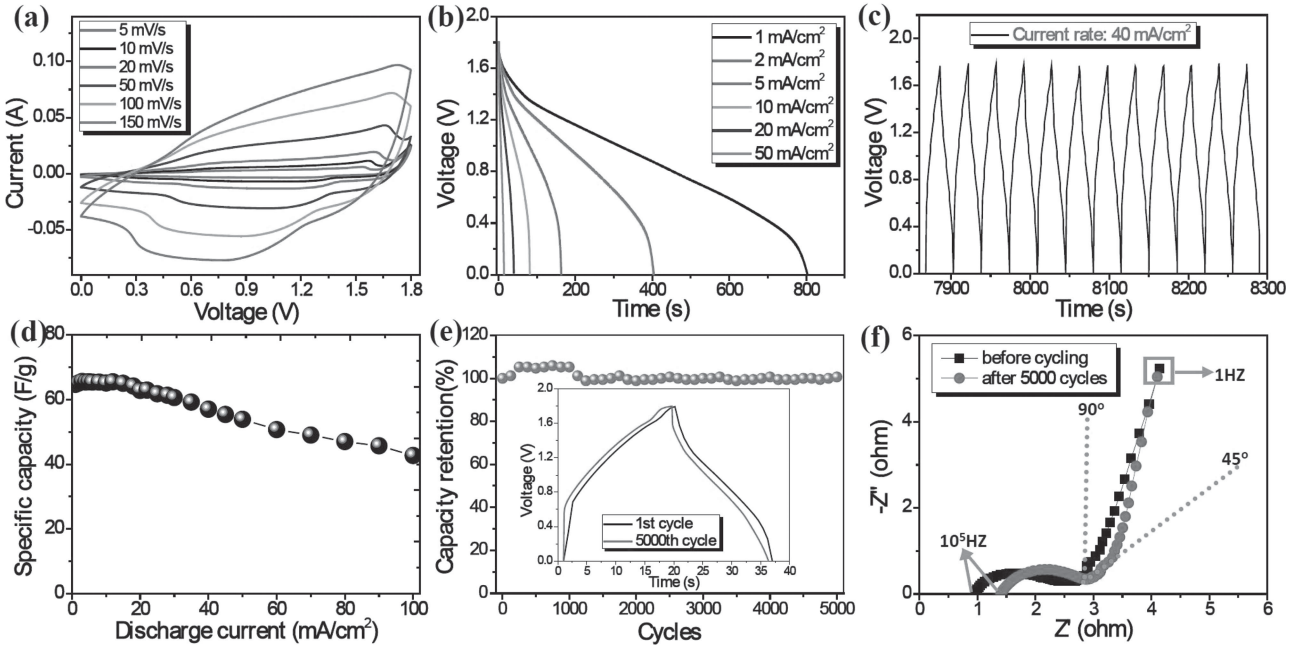

Figure 6. a) Cyclic voltammograms of an optimized asymmetric supercapacitor measured at different scan rates in 3 M KOH electrolyte. b) Discharge curves of the asymmetric supercapacitor at different current densities. c) Charge/discharge curves of the asymmetric supercapacitor at a current rate of 40 mA/cm^2. d) Specific capacitance at different scan rates for the asymmetric capacitor. e) Cycle performance of the asymmetric supercapacitor in a voltage window of approximately 0–(+1.8) V at a scan rate of 40 mA/cm^2. Inset: charge/discharge curves of the first and the 5000th cycle for the asymmetric supercapacitor. f) EIS spectra of the first and the 5000th cycle for the asymmetric supercapacitor.

behavior for the C/$CoNi_3O_4$//AC supercapacitor. The specific capacitance measured at various scan rates are calculated on the basis of the total mass of active materials in both electrodes. As shown in Figure 6d, the maximum specific capacitance that can be achieved is ~64.7 F/g under a scan rate of 1 mA/cm^2. Strikingly, when the current rate increases up to 18 mA/cm^2, it can deliver a specific capacitance of 64.2 F/g (almost no capacitance decay). Even when the current rises up to 100 mA/cm^2 (100 times that of pristine 1 mA/cm^2), its specific capacitance continues to remain as high as 42.7 F/g (~65% capacitance retention). Aside from the rate capability, the cycle lifetime is also a key parameter for supercapacitors. The C/$CoNi_3O_4$//AC asymmetric supercapacitor was cycled between 0 and 1.8 V at a high current density of 40 mA/cm^2 for 5000 cycles. Figure 6d shows the capacitance retention ratio of the asymmetric capacitor as a function of cycle numbers. Less than 1% capacitance decay is observed after the cell underwent 5000 cycles, indicating the excellent long-term stability of this asymmetric supercapacitor. The result is also confirmed by the almost overlapped charge/discharge curves between the first and the 5000th cycles (Figure 6e, inset). Electrochemical impedance spectroscopy (EIS) measurements were conducted for in-depth understanding of the electrochemical behavior of the C/$CoNi_3O_4$//AC asymmetric supercapacitor. Corresponding Nyquist plots in the frequency range of approximately 100 kHz to 0.1 Hz before cycling and after 5000 cycles were recorded (Figure 6f). Both the impedance spectra are similar in shape with an arc at the higher frequency and a spike at the lower frequency, with the exception of the small change of equivalent series resistance (ESR) in the high-frequency (100 kHz) range; this represents a combined resistance from the ionic resistance of the electrolyte and the intrinsic/contact resistance caused by the interfaces.[27] The ESR values before cycling and after 5000 cycles are measured to be ~0.96 and 1.40 Ω, respectively, further providing evidence for the excellent electrochemical cycling stability of the C/$CoNi_3O_4$//AC supercapacitor.

Two additional crucial factors in evaluating supercapacitor performance are the energy density ($E = 1/2CV^2$) and power density ($P = E/t$, where t is time).[28] The Ragone plot of the C/$CoNi_3O_4$//AC supercapacitor has been made to describe the relationship between E and P (see **Figure 7**). Our asymmetric supercapacitor can exhibit an energy density of 29.1 W·h/kg with a power density of 130.4 W/kg at a current rate of 1 mA/cm^2. Noteworthy is that even at a high scan rate of 100 mA/cm^2, its energy density still remains at 19.2 W·h/kg at a power density of 13.0 kW/kg. Considering the energy and power densities, our C/$CoNi_3O_4$//AC asymmetric supercapacitor achieves preferable performance when compared with symmetric supercapacitors, such as AC//AC (2.2 W·h/kg at 4 kW/kg), carbon nanotube (CNT)// CNT (~5 W·h/kg at 100 W/kg) and graphene//graphene (6.7 W·h/kg at 3.3 kW/kg) supercapacitors.[29–31] Additionally, our device has superior performance even when compared with other asymmetric supercapacitors, such as Ni-Co oxide/graphene//AC (7.6 W·h/kg at 5600 W/kg) and NiO//carbon (~10 W·h/kg at 100 W/kg).[32,33] Furthermore, while aiming to investigate the potential for real applications, a 1 cm × 4 cm C/$CoNi_3O_4$//AC supercapacitor device was fabricated by adopting a piece of filter paper as the separator and 3 m KOH as electrolyte. After charging to 3.4 V for less than 1 min, two series supercapacitors can simultaneously light four light-emitting diode (LED) indicators—red (1.76 V, 20 mA), yellow (1.80 V, 20 mA), green (2.36 V, 20 mA), and

© 2014 Wiley-VCH Verlag GmbH & Co. KGaA, Weinheim
small 2014,
DOI: 10.1002/smll.201302937

NANO MICRO small

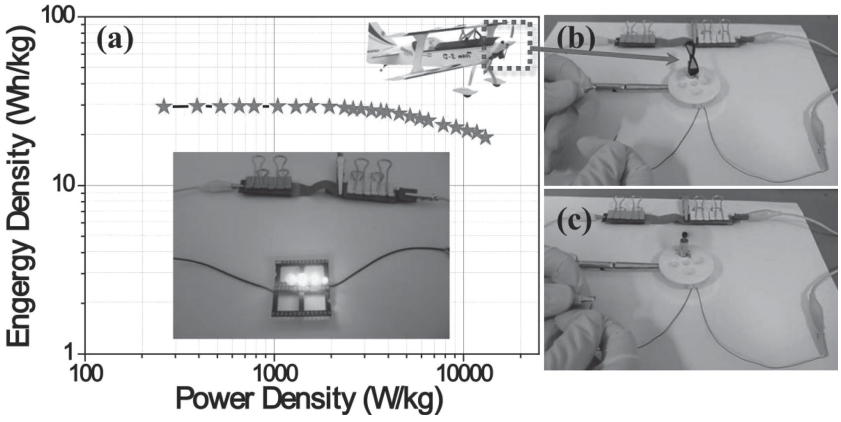

Figure 7. a) Ragone plot of C/$CoNi_3O_4$//AC asymmetric supercapacitor. Inset: optical image of two supercapacitors in series lighting four differently colored LED indicators. b,c) Optical images showing the two supercapacitors in series driving the motor of remote-controlled planes (2 V, 0.56 A).

blue (2.50 V, 20 mA), as obviously shown in the inset of Figure 7. More strikingly, the as-made supercapacitor device can also robustly power the motor (2 V, 0.56 A) of remote-controlled model planes after a few seconds of charging (Figure 7a,b and video in the Supporting Information), which suggests the remarkable potential of C/$CoNi_3O_4$ NAs in high-power-delivery applications.

3. Conclusion

In summary, the electrode of 3D network-like C/$CoNi_3O_4$ NAs was built on a stainless steel substrate via a two-step approach, and it demonstrated outstanding pseudocapacitive behavior, with an ultrahigh capacitance of ~1299 F/g (~1429 mF/cm^2) at 0.5 mA/cm^2 and an excellent rate performance (~78% capacity retention when the current was increased by 100 times). Increased accessible surface area is provided by the mesoporous structure; the facile ion-diffusion path and fast electronic transfer superhighway rendered by the 3D network architecture give rise to the excellent electrochemical performance. An optimized asymmetric supercapacitor based on the synthesized C/$CoNi_3O_4$ NAs and AC was also developed. Our asymmetric supercapacitor can work in a high potential range of approximately 0–(+1.8) V, showing a specific capacitance of 64.7 F/g at a current rate of 1 mA/cm^2. Strikingly, even when the scan rate is increased up to 100 mA/cm^2, it can still deliver a capacitance of 42.7 F/g, with an energy density of 19.2 W·h/kg and a power density of 13.0 kW/kg. Moreover, the supercapacitor device exhibits excellent long cycle life with less than 1% specific capacitance decay after 5000 cycles. Additionally, within seconds of charging, two asymmetric supercapacitors connected in series can simultaneously power four differently colored LED indicators or even drive the motor of remote-controlled model planes. This confirms its potential for use in practical applications. This work paves the way for developing complex nanostructured electrodes to advance the design and fabrication of high-performance asymmetric supercapacitors.

4. Experimental Section

Sample Synthesis: The 3D C/$CoNi_3O_4$ NAs were synthesized via a facile hydrothermal approach followed by glucose coating and calcination treatment in an Ar atmosphere. In detail, 0.7 g $Ni(NO_3)_2{\cdot}6H_2O$ (Sigma, Aldrich), 0.4 g $Co(NO_3)_2{\cdot}6H_2O$ (Sigma, Aldrich), 0.2 g NH_4F (Sigma, Aldrich), and 0.75 g $CO(NH_2)_2$ (Sigma, Aldrich) were successively dissolved in 50 mL deionized water with magnetic stirring at room temperature. After 10 min, the homogeneous solution was transferred to a 100-mL Teflon-lined autoclave with a piece of clean Fe-Co-Ni alloy (200 mm × 400 mm × 0.3 mm; atomic ratio of Fe:Co:Ni = 52.23:18.07:29.7) immersed into the reaction solution. The autoclave was sealed and maintained at 120 °C for 4 h, and then cooled down to room temperature. The cobalt-nickel hydroxide carbonate precursor grown on the Fe-Co-Ni substrate was removed, rinsed with distilled water several times, and dried in air at 60 °C. For carbon modification, the as-prepared precursor film was immersed into a 0.3 m glucose solution in a 60 °C electric oven for 3 h and further annealed under Ar flow (80 sccm) at 500 °C for 90 min.

Sample Characterization: XRD measurements were adopted to check the phase structures of the prepared samples on a Bruker D-8 Advance diffractometer using Cu $K\alpha$ radiation (λ = 1.5418 Å). SEM and TEM/HRTEM were also conducted to analyze the crystalline structure and morphology of the samples using a JEOL JSM-6700F field-emission scanning electron microscope and a JEM 2010 transmission electron microscope, respectively. Raman spectroscopy was carried out with a Witech CRM200 instrument (532 nm) to characterize the products. The specific surface area and pore size of the final product were determined using nitrogen-adsorption/-desorption isotherms with a BELSORP analyzer (JP. BELCo. Ltd) at 77 K. The mass loading of the active material was carefully weighed on a microbalance with an accuracy of 0.1 mg (A&D Company N92, Japan). On average, ~1.10 mg of the C/$CoNi_3O_4$ NAs was statistically determined to be on an area of 1 cm × 1 cm of alloy substrate.

Electrochemical Measurements: Electrochemical measurements were performed at room temperature on an electrochemical workstation (CHI 760D, CHI Instruments Inc., Shanghai) in 3 m KOH aqueous solution. For the three-electrode electrochemical system, a platinum plate and a calomel electrode (SCE) served as the counter-electrode and reference electrode, respectively. After encapsulation (the edges of the electrodes were sealed by epoxy resin), the C/$CoNi_3O_4$ NAs on the Fe-Co-Ni substrate were used directly as the working electrode. Prior to electrochemical measurements, each electrode was pre-activated by 500 CV cycles (scanning rate: 50 mV/s). The areal and specific capacitance was calculated using $C_a = I{\times}t/(S{\times}\triangle V)$ and $C_s = I{\times}t/(m{\times}\triangle V)$, respectively, where I is the discharging current, t is the discharging time, $\triangle V$ is the voltage drop upon discharging (excluding the IR drop), S is the geometrical area of the electrode, and m is the total mass of the active material.[34]

The asymmetric supercapacitor was made of a C/$CoNi_3O_4$ NAs cathode and an AC-based anode. The AC-based anode was

DOI: 10.1002/smll.201302937
© 2014 Wiley-VCH Verlag GmbH & Co. KGaA, Weinheim

prepared by mixing 85 wt% AC (Black Pearl 2000, Cabot), 10 wt% acetylene black, and 5 wt% polyvinylidene fluoride (PVDF) with dimethylformamide (DMF) to form the slurry, which was then spread onto nickel foams and dried at 80 °C in an electric oven. The loading mass of AC was measured to be 5.8 mg/cm^2. During tests of the C/$CoNi_3O_4$//AC asymmetric supercapacitor, the area of the electrode surface was approximately 0.5 cm × 2 cm. The specific capacitance (F/g), energy density (W·h/kg), and power density (W/Kg) values were calculated based on the total mass of active materials on both of the electrodes. Electrochemical impedance spectroscopy (EIS) measurements were carried out by applying an alternating-current voltage with a 5 mV amplitude in a frequency range from 0.1 Hz to 100 kHz.

Supporting Information

Supporting Information is available from the Wiley Online Library or from the author.

Acknowledgements

This work is supported by the Singapore National Research Foundation under NRF RF Award No. NRF-RF2010–07. H.Z. acknowledges the support from the MOE under AcRF Tier 2 (ARC 10/10, No. MOE2010-T2–1–060), AcRF Tier 1 (RG 61/12), and Start-Up Grant (M4080865.070.706022); and the National Research Foundation under the Campus for Research Excellence and Technological Enterprise (CREATE).

[1] a) P. Simon, Y. Gogotsi, *Nat. Mater.* **2008**, *7*, 845; b) J. R. Miller, P. Simon, *Science* **2008**, *321*, 651; c) J. Jiang, Y. Y. Li, J. P. Liu, X. T. Huang, C. Z. Yuan, X. W. Lou, *Adv. Mater.* **2012**, *24*, 5166.

[2] a) X. H. Lu, M. H. Yu, G. M. Wang, T. Zhai, S. L. Xie, Y. C. Ling, Y. X. Tong, Y. Li, *Adv. Mater.* **2013**, *25*, 267; b) X. Xiao, T. Q. Li, P. H. Yang, Y. Gao, H. Y. Jin, W. J. Ni, W. H. Zhan, X. H. Zhang, Y. Z. Cao, J. W. Zhong, L. Gong, W.-C. Yen, W. J. Mai, J. Chen, K. F. Huo, Y. L. Chuen, Z. L. Wang, J. Zhou, *ACS Nano* **2012**, *6*, 9200.

[3] a) Y. P. Fu, X. Cai, H. W. Wu, Z. B. Lv, S. C. Hou, M. Peng, X. Yu, D. C. Zou, *Adv. Mater.* **2012**, *24*, 5713; b) L. H. Bao, X. D. Li, *Adv. Mater.* **2012**, *24*, 3246.

[4] a) J. Jiang, J. P. Liu, W. W. Zhou, J. H. Zhu, X. T. Huang, X. Y. Qi, H. Zhang, T. Yu, *Energy Environ. Sci.* **2011**, *4*, 5000; b) L. Q. Mai, F. Yang, Y. L. Zhao, X. Xu, L. Xu, Y. Z. Luo, *Nat. Commun.* **2011**, *2*, 381; c) C. Guan, X. L. Li, Z. L. Wang, X. H. Cao, C. Soci, H. Zhang, H. J. Fan, *Adv. Mater.* **2012**, *24*, 4186.

[5] a) J. Xu, Q. F. Wang, X. W. Wang, Q. Y. Xiang, B. Liang, D. Chen, G. Z. Shen, *ACS Nano* **2013**, *7*, 5432; b) J. Yan, Z. J. Fan, W. Sun, G. Q. Ning, T. Wei, Q. Zhang, R. F. Zhang, L. J. Zhi, F. Wei, *Adv. Funct. Mater.* **2012**, *22*, 2632; c) J. T. Zhang, J. W. Jiang, H. L. Li, X. S. Zhao, *Energy Environ. Sci.* **2011**, *4*, 4009.

[6] a) P.-C. Chen, G. Z. Shen, Y. Shi, H. T. Chen, C. W. Zhou, *ACS Nano* **2012**, *4*, 4403; b) Z. P. Sun, S. Firdoz, E. Y.-X. Yap, L. Li, X. M. Lu, *Nanoscale* **2013**, *5*, 4379.

[7] a) X. Zhao, L. L. Zhang, S. Murali, M. D. Stoller, Q. H. Zhang, Y. W. Zhu, R. S. Ruoff, *ACS Nano* **2012**, *6*, 5404; b) Y. G. Wang, Z. S. Hong, M. D. Wei, Y. Y. Xia, *Adv. Funct. Mater.* **2012**, *22*, 5185.

[8] a) C. Zhou, Y. W. Zhang, Y. Y. Li, J. P. Liu, *Nano Lett.* **2013**, *13*, 2078; b) Z.-S. Wu, Y. Sun, Y.-Z. Tan, S. B. Yang, X. L. Feng, K. Müllen, *J. Am. Chem. Soc.* **2012**, *134*, 19532.

[9] a) C. Z. Yuan, J. Y. Li, L. R. Hou, X. G. Zhang, L. F. Shen, X. W. Lou, *Adv. Funct. Mater.* **2012**, *22*, 4592; b) X. Wang, A. Sumboja, M. F. Lin, J. Yan, P. S. Lee, *Nanoscale* **2012**, *4*, 7266.

[10] a) C.-C. Hu, L. C. Chen, K.-H. Chang, *J. Power Sources* **2013**, *221*, 128; b) W. W. Zhou, J. P. Liu, T. Chen, K. S. Tan, X. T. Jia, Z. Q. Luo, C. X. Cong, H. P. Yang, C. M. Li, T. Yu, *Phys. Chem. Chem. Phys.* **2011**, *13*, 14462.

[11] a) Z. Tang, C.-H. Tang, H. Gong, *Adv. Funct. Mater.* **2012**, *22*, 1272; b) D.-W. Wang, F. Li, H.-M. Cheng, *J. Power Sources* **2008**, *185*, 1563; c) J. P. Liu, C. W. Cheng, W. W. Zhou, H. X. Li, H. J. Fan, *Chem. Commun.* **2011**, *47*, 3436.

[12] a) H. L. Wang, Q. M. Gao, L. Jiang, *Small* **2011**, *7*, 12454; b) H. Jiang, J. Ma, C. Z. Li, *Chem. Commun.* **2012**, *48*, 4465; c) X. H. Liu, R. Z. Ma, Y. S. Bando, T. Sasaki, *Adv. Mater.* **2012**, *24*, 2148.

[13] a) J. Chang, J. Sun, C. H. Xu, H. Xu, L. Gao, *Nanoscale* **2012**, *4*, 6786; b) C. H. Tang, Z. Tang, H. Gong, *J. Electrochem. Soc.* **2012**, *159*, A651.

[14] a) X. F. Wang, B. Liu, Q. F. Wang, W. F. Song, X. J. Hou, Y.-B. Cheng, G. Z. Shen, *Adv. Mater.* **2013**, *25*, 1479; b) J. Jiang, Y. Y. Li, J. P. Liu, X. T. Huang, *Nanoscale* **2011**, *3*, 45; c) J. Y. Ji, L. L. Zhang, H. X. Ji, Y. Li, X. Zhao, X. Bai, X. B. Fan, F. B. Zhang, R. S. Ruoff, *ACS Nano* **2013**, *7*, 6237.

[15] a) E. Lyyamperumal, S. Y. Wang, L. M. Dai, *ACS Nano* **2012**, *6*, 5259; b) J. T. Li, W. Zhao, F. Q. Huang, A. Manivanan, N. Q. Wu, *Nanoscale* **2011**, *3*, 5103; c) J. H. Zhong, A.-L. Wang, G.-R. Li, J.-W. Wang, Y.-N. Ou, Y. X. Tong, *J. Mater. Chem.* **2012**, *22*, 5656.

[16] a) Y. S. Luo, J. Jiang, W. W. Zhou, H. P. Yang, J. S. Luo, X. Y. Qi, H. Zhang, D. Y. W. Yu, C. M. Li, T. Yu, *J. Mater. Chem.* **2012**, *22*, 8634; b) J. S. Luo, X. H. Xia, Y. S. Luo, C. Guan, J. L. Liu, X. Y. Qi, C. F. Ng, T. Yu, H. Zhang, H. J. Fan, *Adv. Energy Mater.* **2013**, *3*, 737.

[17] a) H. G. Zhang, X. D. Yu, P. V. Braun, *Nat. Nanotechnol.* **2011**, *6*, 277; b) J. P. Liu, J. Jiang, C. W. Cheng, H. X. Li, J. X. Zhang, H. Gong, H. J. Fan, *Adv. Mater.* **2011**, *23*, 2076.

[18] a) J. H. Zhu, J. Jiang, Y. M. Feng, G. X. Meng, H. Ding, X. T. Huang, *ACS Appl. Mater. Interfaces* **2013**, *5*, 2634; b) J. Jiang, J. H. Zhu, Y. M. Feng, J. P. Liu, X. T. Huang, *Chem. Commun.* **2012**, *48*, 7471.

[19] J. Jiang, J. P. Liu, X. T. Huang, Y. Y. Li, R. M. Ding, X. X. Ji, Y. Y. Hu, Q. B. Chi, Z. H. Zhu, *Cryst. Growth Des.* **2010**, *10*, 70.

[20] H.-C. Chien, W.-Y. Cheng, Y.-H. Wang, S.-Y. Lu, *Adv. Funct. Mater.* **2012**, *22*, 5038.

[21] J. H. Zhu, J. Jiang, J. P. Liu, R. M. Ding, Y. Y. Li, H. Ding, Y. M. Feng, G. M. Wei, X. T. Huang, *RSC Adv.* **2011**, *1*, 1020.

[22] G. X. Hu, C. H. Tang, C. X. Li, H. M. Li, Y. Wang, H. Gong, *J. Electrochem. Soc.* **2011**, *158*, A695.

[23] a) B. Liu, D. S. Tan, X. F. Wang, D. Chen, G. Z. Shen, *Small* **2013**, *9*, 1998; b) J. Jiang, J. P. Liu, R. M. Ding, J. H. Zhu, Y. Y. Li, A. Z. Hu, X. Li, X. T. Huang, *ACS Appl. Mater. Interfaces* **2011**, *3*, 99.

[24] a) B. Liu, J. Zhang, X. F. Wang, G. Chen, C. W. Zhou, G. Z. Shen, *Nano Lett.* **2012**, *12*, 3005; b) W. W. Zhou, J. P. Liu, T. Chen, K. S. Tan, X. T. Jia, Z. Q. Luo, C. X. Cong, H. P. Yang, C. M. Li, T. Yu, *Phys. Chem. Chem. Phys.* **2011**, *13*, 14462.

[25] L. L. Zhang, X. Zhao, H. X. Ji, M. D. Stoller, L. F. Lai, S. Murali, S. Mcdonnell, B. Cleveger, R. M. Wllace, R. S. Ruoff, *Energy Environ. Sci.* **2012**, *5*, 9618.

[26] Q. F. Wang, X. F. Wang, B. Liu, G. Yu, X. J. Hou, D. Chen, G. Z. Shen, *J. Mater. Chem. A* **2013**, *1*, 2468.

© 2014 Wiley-VCH Verlag GmbH & Co. KGaA, Weinheim

DOI: 10.1002/smll.201302937

[27] J. P. Liu, C. W. Cheng, W. W. Zhou, H. X. Li, H. J. Fan, *Chem. Commun.* **2011**, *47*, 3436.
[28] Y. Y. Li, Z. S. Li, P. K. Shen, *Adv. Mater.* **2013**, *25*, 2474.
[29] D.-W. Wang, F. Li, M. Liu, G. Q. Lu, H. M. Cheng, *Angew. Chem. Int. Ed.* **2008**, *47*, 373.
[30] C. J. Yu, C. Masarapu, J. P. Rong, B. Q. Wei, H. Q. Jiang, *Adv. Mater.* **2009**, *21*, 4793.
[31] H. L. Wang, Y. Y. Liang, T. Mirfakhrai, Z. Chen, H. S. Casalongue, H. J. Dai, *Nano Res.* **2011**, *4*, 729.
[32] H. L. Wang, C. M. B. Holt, Z. Li, X. H. Tan, B. S. Amirkhiz, Z. W. Xu, B. C. Olsen, T. Stephenson, D. Mitlin, *Nano Res.* **2012**, *5*, 605.
[33] H. Inoue, Y. Namba, E. Higuchi, *J. Power Sources* **2010**, *195*, 6239.
[34] C. Guan, J. P. Liu, C. W. Cheng, H. X. Li, X. L. Li, W. W. Zhou, H. Zhang, H. J. Fan, *Energy Environ. Sci.* **2011**, *4*, 4496.

Received: September 11, 2013
Published online:

© 2014 Wiley-VCH Verlag GmbH & Co. KGaA, Weinheim